Sensor network based PV power nowcasting with spatio-temporal preselection for grid-friendly control

Xiaoyang Chen[a], Yang Du[b,*], Enggee Lim[a], Huiqing Wen[a], Lin Jiang[c]

[a] *Xi'an-Jiaotong Liverpool University, China*
[b] *James Cook University, Australia*
[c] *The University of Liverpool, United Kingdom*

Abstract

The increasing penetration of photovoltaics (PV) systems introduces more uncertainties to the power system, and has drawn serious concern for maintaining the grid stability. Consequently, the PV power grid-friendly control (GFC) has been imposed by utilities to provide additional flexibilities for power system operations. Conventional GFC strategies show limitations to estimate real-time maximum available power, especially when fast moving clouds occur. In this regards, the spatio-temporal (ST) PV nowcasting using a sensor network provides a remedy to the above issue. However, current ST nowcasting methods suffer from the problems such as predictor mis-selection, inconsistent nowcasting, and poor model adaptability, which still hinder their practical use for GFC. In this paper, a novel ST PV power nowcasting method with predictor preselection is presented, which can be used for GFC. The proposed method enables a fast and precise predictor preselection in different scenarios, and provides consistent PV nowcasts with cloud information interpolated. The effectiveness of the proposed nowcasting method is evaluated in a real sensor network. The experimental results reveal that the proposed method has strong robustness in case of various weather conditions, with fewer training data used. Compared with the conventional methods, the proposed method shows an average nRMSE and nPMAE improvements over 13.5% and 41.3% respectively in the cloudy days. A practice of integrating the proposed nowcasting method to GFC operation is also demonstrated. The results show that the proposed method is promising to improve the performance of GFC.

Keywords: PV nowcasting, Sensor network, Predictor preselection, Grid-friendly control

1. Introduction

Renewable energy particularly solar photovoltaic (PV) energy is becoming an important source for power generation, and gaining global popularity in recent years [1]. As the cost of PV generation plummets, PV power is reaching grid parity in many countries, with a levelized cost equal or lower than the non-renewable electricity tariffs [2]. In this context, it opens up more opportunities to integrate PV systems into grid. Nonetheless, as it may be perceived as an inconsistent resource, PV power raises a series of grid steady-state operation issues due to the difficulty to dispatch that energy [3]. Moreover, in terms of dynamics, the intermittent PV generation that is mainly resulted from the movement of clouds causes power fluctuations in grid. When the penetration is low, the fluctuating power can be directly absorbed by the grid in the form of insignificant frequency deviations. When a large-scale PV system or accumulated high penetration is concerned, these fluctuations can damage the grid frequency balance, and eventually lead to harmonic distortion even blackouts [4]. In order to tackle the above challenges, several power utilities have imposed standards to control the PV output power from intermittent generation [5, 6, 7]. As a result, PV power grid-friendly control (GFC) such as power limiting control, power ramp-rate control, and power reserve control have been proposed, where the PV power is actively curtailed or reserved to provide more flexibilities to the grid [8, 9]. However, sudden changes in solar irradiance can introduce more uncertainties to the power production, and it becomes more challenging for the control to suppress sufficient reserved power to comply with the standard regulation. In this sense, having the knowledge of the amount of expected produced PV power becomes crucial. If the solar irradiance and the projected power generation can be forecasted for the near future, it is possible to implement GFC in a more effective way.

In the modern power system, PV power forecasting have been widely exploited to facilitate a smarter grid steady-state operation, such as demand side management, reserve capacity planning, and economical dispatching. For these applications, forecasting methods typically process and make predictions at a large spatial aggregation (a regional system) with hourly or daily resolution, which are referred as mid-term or long-term forecasting [10, 11, 12].

*Corresponding author
Email address: yang.du@jcu.edu.au (Yang Du)

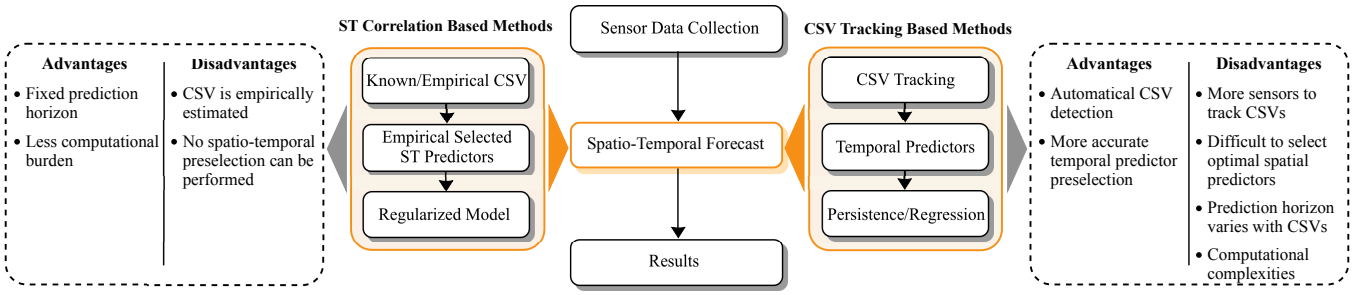

Figure 1: Summary of conventional ST nowcasting methods using a sensor network. Two categories can be identified according to the way of extracting cloud information.

With regard to GFC application, however, forecasts at lower spatial aggregation (an individual PV system) with higher temporal resolution (a few seconds to several minutes) are expected, where the PV variability is smoothed much less and the local cloud shading becomes more important [13, 14, 15]. This is known as the PV nowcasting.

1.1. State-of-art PV nowcasting methods

PV nowcasting, also referred as ultra short-term PV forecasting are primarily obtained by determining the motion of local clouds [16]. Sky camera is one of the most commonly used approach for PV nowcasting [17, 18, 19, 20, 21]. Although the sky camera approach has an advantage in providing cloud position information, difficulty rises during the conversion from cloud conditions to ground level irradiance. The main sources of errors are the inaccurate cloud base height approximation and cloud contour extraction near the solar disk. Occurrence of haze, which is often falsely identified as thin clouds, may also contribute to nowcasting errors [22]. Alternatively, the spatio-temporal (ST) nowcasting using data from a sensor network overcomes the challenges that typically associated with the sky camera based approaches, such as the cloud height estimation and pixel-irradiance conversion. As clouds propagate over the sensor network, one can preselect sufficient lagged time series data (temporal predictors) collected by the neighboring sensors (spatial predictors) as predictors for the focal location. Depending on how the cloud information is coupled, the ST nowcasting can be subdivided into two categories: cloud tracking based methods and ST correlation based methods.

The cloud tracking based methods aim to describe the cloud information with cloud shadow vector (CSV). PV nowcasts are then produced by transposing the generated power map in the direction of CSV. Various CSV tracking strategies have been introduced in the literature, such as the most-correlated pair method [23, 24, 25], and peak matching method [26]. The main advantage of using the cloud tracking based method is that it provides an accurate measure of the time lag between the measured data at the sensors and focal PV system. In another word, the temporal predictors can be adequately preselected. However, these methods often produce nowcasts of variable prediction horizon, which is limited by the network dimension and CSV velocity [27]. Although a peer-to-peer method is proposed in [28] to provide consistent PV nowcasts with a fixed prediction horizon, numerous PV references (202 rooftop systems) over a wide geographic dispersion (≈ 1400 km^2) are required. Furthermore, a simple persistence model or multivariate regression model is typically used in these methods, which often includes insufficient or irrelevant spatial predictors. Consequently, the model becomes inferior to adapt various CSVs [22].

Instead of explicitly deriving the CSV, ST correlation based methods consider the cloud information indirectly. PV nowcasts are generated by exploiting the ST correlations observed among the predictors. However, the number of predictors can become very large as the number of sensors in the network increases. In this situation, several works have implemented the regularized model such as the lasso (least absolute shrinkage and selection operator) for parameter shrinkage [29, 30, 31], which is able to filter out the highly correlated predictors. The prediction horizon using these methods can be set as a fixed value, which equals to the resolution of training data. However, the methods listed above only consider the homogeneous CSV impacts through both space and time, and depend on known or empirically estimated CSV movements. When the CSV changes frequently, the model may fail to timely adapt the cloud dynamics, leading to the inclusion of both irrelevant spatial and temporal predictors. As a result, the nowcasting performance becomes much worse [32].

Figure 1 demonstrates the flowchart of the two conventional ST nowcasting methods. As previously discussed, these methods have shown some limitations in terms of:

1. Lack of a fast and comprehensive preselection mechanism for both spatial and temporal predictors.

2. Difficulties to provide consistent PV nowcasts with a fixed prediction horizon while maintaining cloud dynamics.

3. Poor model robustness to adapt frequent CSV changes.

To address the above issues, a scenario-recognizable preselection (SRP) framework is developed for PV now-

casting. The proposed SRP method establishes a comprehensive ST predictor preselection framework, which enables most-relevant predictors to be selected in absence or presence of CSVs. PV nowcasts with a constant prediction horizon is achieved using a regularized model elastic-net, and complemented by the CSV tracking results when CSV is detectable. The effectiveness of the SRP based elastic-net (SRP-Enet) model is validated on a real sensor network from November 1, 2018 to April 1, 2019, and a total of 5 case studies are presented for detailed evaluation. Compared with other commonly-used PV nowcasting methods, the proposed method significantly improves the nowcasting accuracy, with the feature that the predicted values approach closer to the actual ramp peaks. A practical application of integrating the nowcasts to GFC operation is also provided to verify the feasibility of the proposed method.

The remaining of the paper is organized as following. After describing the deployment of the sensor network in Section 2, we introduce the proposed SRP-Enet nowcasting method in Section 3. Section 4 then presents the results of the proposed method, with 5 case studies evaluated. Afterwards, a practical application of using the nowcasts for GFC is demonstrated in Section 5. Finally, we conclude the paper in Section 6.

2. Sensor network description

For a proper design of a sensor network, it is supposed to provide online and high sampling measurements with appropriate spatial resolution to support PV nowcasting applications. The network should also be able to capture the omnidirectional CSVs. Additionally, it should demand a flexible infrastructure and low investment in order to be coupled with various PV systems.

In this work, a concentric sensor network configuration with two cross layers is adopted. The sensor developed herein is made from a mini solar cell. From each sensor, the short-circuit current of the solar cell is measured at 1-s resolution, and mapped to the corresponding global horizontal irradiance (GHI) data through a previously tuned conversion model. The converted GHI data is then packed and sent to the local server via LoRa wireless communication. More details about the sensor development can be found in Appendix A. Figure 2 shows an example layout of the sensor network, where the focal PV system covers a surface of 0.15 km^2, and rated at 5 MW. In order to reduce the packet loss rate and data transfer delays, an optimal wireless communication distance is found to be within 500 m. In addition, to prevent a single CSV fleeing between the sensor separations, the distance between two adjacent sensors should be less than 200 m, which is the case for a common CSV length [16]. With the above considerations, totally 32 sensors would be deployed and enclose the whole PV system to capture the omnidirectional CSVs, with 16 exterior sensors and 16 interior sensors, separated by around 60 m. For a sensor sampling time of 1 s, the largest detectable CSV velocity reaches 60 m/s, which should cover most weather conditions (greater than 50 m/s is very unlikely [33]).

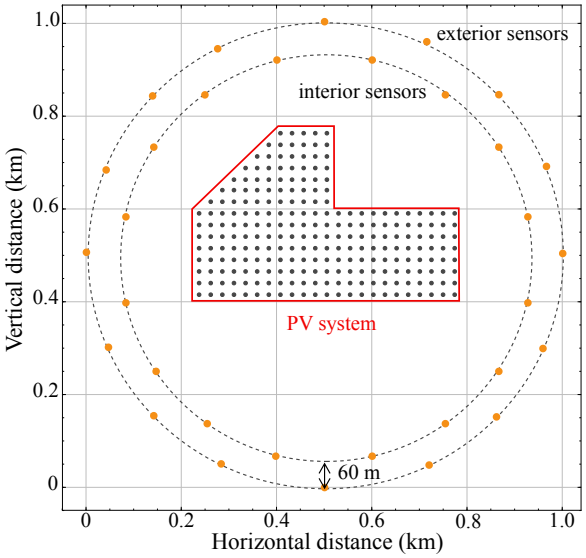

Figure 2: Concentric network configuration example of a 5 MW PV system, covering a surface of 0.15 km^2. Totally 32 sensor are used to enclose the PV system (16 exterior sensors, and 16 interior sensors). Distance between the exterior and interior layer is around 60 m.

Compared with other network configurations mentioned in [24, 25, 26, 28], the developed sensor network greatly reduces the required sensor numbers and geographical dispersion. More importantly, it is easy to be generalized and adapted to different PV systems. Last but not least, the network is flexible, and one can conveniently add or remove sensors, even a layer.

3. Proposed SRP-Enet nowcasting method

The flowchart of the proposed SRP-Enet nowcasting method is shown in Figure 3. It has been pointed out that the nowcasting performance can be highly dependent on the ability to capture the ST dynamical components of the irradiance field [22]. In this regards, the nowcasting method proposed herein decomposes the irradiance dynamics into two scenarios, namely, ramp scenarios where there are high possibilities for PV power fluctuations, and stationary scenarios where more smoothed PV generation is likely to be produced. Then two different ST predictor preselection approaches are implemented based on the scenario recognition. The consistent PV nowcasts with a fixed prediction horizon is provided in stationary scenarios, and complemented by the nowcasts in ramp scenarios when CSV is available. A detailed description of the proposed method is presented as following.

3.1. Scenario recognition

Suppose $\Phi = \{S_1, S_2, \ldots, S_N\}$ is the complete set of a sensor network, where S_i represents a single sensor, and

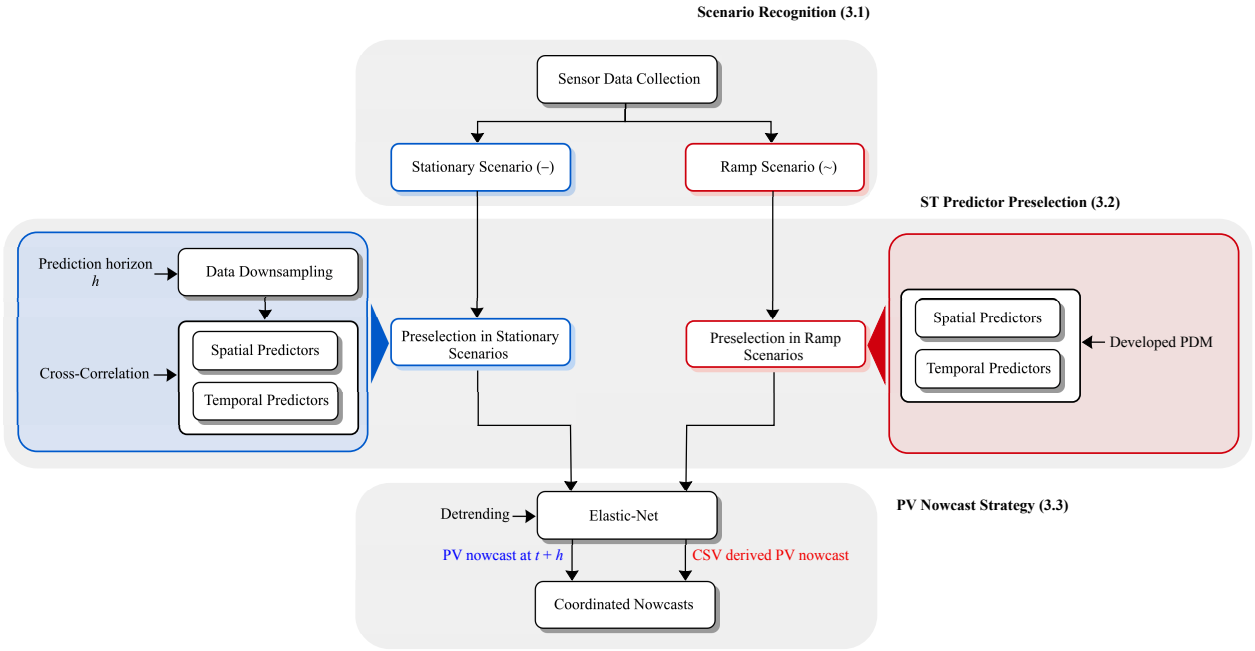

Figure 3: A complete flowchart of the proposed SRP-Enet nowcasting method. The proposed method consists of three main blocks, namely scenario recognition, ST predictor preselection, and PV nowcast strategy. The numbers between parentheses indicate the corresponding sections for detailed description.

$N = \text{card}(\Phi)$ denotes the cardinality of the set, indicating the overall sensor numbers. Φ^{ext} and Φ^{int} represent two subsets, namely the exterior sensor set and interior sensor set respectively, where $N^{ext} = \text{card}(\Phi^{ext})$, $N^{int} = \text{card}(\Phi^{int})$, and $N^{ext} + N^{int} = N$. Given the instantaneous measurements of two sensors i, j at time t being $x_{i,t}$ and $x_{j,t}$, two scenarios are defined as:

Stationary scenario: A stationary scenario will be identified if the absolute measurements difference between arbitrary two sensors in the network is less than a predefined threshold value P_{th}:

$$\forall\ i, j \in \Phi,\ |x_{i,t} - x_{j,t}| \leq P_{th} \tag{1}$$

Ramp scenario: A ramp scenario will be identified if there exists a pair of exterior sensor and interior sensor whose absolute measurements difference is greater than a predefined threshold value P_{th}:

$$\exists\ i \in \Phi^{ext},\ j \in \Phi^{int},\ |x_{i,t} - x_{j,t}| > P_{th} \tag{2}$$

Based on (1) and (2), the real-time sensor data stream is processed and labeled as stationary $\bar{x}_{i,t}$ or ramp $\tilde{x}_{j,t}$, where the hats "$-$" and "$\sim$" denote the stationary scenario and ramp scenario respectively. A scenario recognition signal ζ_t is then generated, given by

$$\zeta_t = \begin{cases} 0, & \text{stationary scenario} \\ 1, & \text{ramp scenario} \end{cases} \tag{3}$$

It should be noticed that a stationary scenario reveals not only a clear-sky condition, but also a sky with complete and heavy cloud coverage, under which a smooth sensor output series can be observed as well. In addition, the recognition of each scenario requires at least two sensor measurement profiles, which enhances the reliability of recognition (the occurrence of simultaneous measurements error by multiple sensors is significantly decreased).

3.2. ST predictor preselection

In ramp scenarios, due to the rapid movements of CSVs, a fast ST predictor preselection algorithm is desired to cope with the cloud dynamics. However, the sensor data in stationary scenarios typically presents to be much more smooth and less featured in fluctuations, which slows the preselection process. If the ramp scenarios share a similar preselection mechanism to stationary scenarios, the cloud information may not be reported in time, leading to insufficient time buffer for GFC preparation. Thus for the proposed SRP method, two different preselection strategies are adopted based on the former scenario recognition.

3.2.1. Preselection in stationary scenarios

For stationary scenario analysis, the 1-s resolution sensor data is first downsampled to h-resolution, since the consistent PV nowcasting with a fixed prediction horizon h is demanded in this scenario. Given the time instant t, the output time series of an arbitrary sensor $i \in \Phi$ and focal PV system can be found by

$$\overline{X}_{i,t}^{T_{obs}} = \begin{bmatrix} \bar{x}_{i,t-T_{obs}} \\ \vdots \\ \bar{x}_{i,t-2h} \\ \bar{x}_{i,t-h} \end{bmatrix},\ \overline{Y}_{t}^{T_{obs}} = \begin{bmatrix} \bar{y}_{t-T_{obs}} \\ \vdots \\ \bar{y}_{t-2h} \\ \bar{y}_{t-h} \end{bmatrix} \tag{4}$$

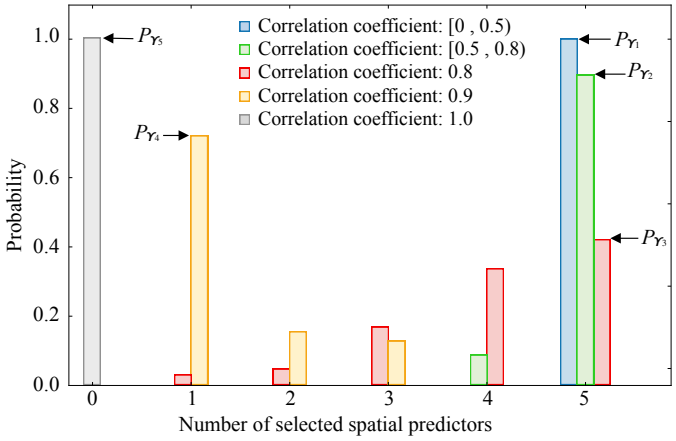

Figure 4: An example of determining the threshold correlation coefficient Υ for a network with 5 sensors. In this case, sensor data collected over 6 hours are used to generate the distribution, leading to the peak probability set $\{P_{\Upsilon_1}, \cdots, P_{\Upsilon_5}\}$. In this case, P_{Υ_3} is found as the minimum value in the set, thus $\Upsilon_3 = 0.8$ is selected as the threshold.

where $\overline{X}_{i,t}^{T_{obs}}$ and $\overline{Y}_{t}^{T_{obs}}$ respectively denote the time series of sensor measurements and focal PV system outputs over an observation window T_{obs}.

To indicate the most-relevant ST predictors among the sensor network, all the sensor series will be shifted in time, and the correlation coefficient is calculated with an increasing time shift $\delta t = -nh, \ldots, -h, 0, h, \ldots, nh$, given by

$$\rho_{i,\delta t} = \frac{Cov(\overline{X}_{i,t+\delta t}^{T_{obs}}, \overline{Y}_{t}^{T_{obs}})}{\sqrt{Var(\overline{X}_{i,t+\delta t}^{T_{obs}})}\sqrt{Var(\overline{Y}_{t}^{T_{obs}})}}, \quad i \in \Phi \tag{5}$$

where $Cov(\cdot)$ and $Var(\cdot)$ indicate the covariance function and variance function respectively.

To effectively filter out the irrelevant sensors, a threshold correlation coefficient Υ is applied. Then only the sensors with $\max(\rho_{i,\delta t}) > \Upsilon$ are selected as spatial predictors. The spatial predictor preselection is formulated by

$$\overline{\Phi} = \{i\}, \quad \text{if } \max(\rho_{i,\delta t}) > \Upsilon, \quad i \in \Phi \tag{6}$$

where $\overline{\Phi}$ represents the stationary spatial predictor set, and $\bar{n}_s = \text{card}(\overline{\Phi})$ denotes the number of spatial predictors.

The selection of threshold value Υ varies case by case, which is mainly dependent on the network configuration, local meteorological conditions, etc. Figure 4 shows an example of finding a proper Υ for a network with 5 sensors. For a group choices of threshold value $\{\Upsilon_1, \Upsilon_2, \cdots, \Upsilon_k\}$, each element will be fed to Equation (6), and the corresponding probability distribution of the selected spatial predictor numbers are calculated. For each probability distribution, the maximum probability value will be recorded, appending to the set $\{P_{\Upsilon_1}, P_{\Upsilon_2}, \cdots, P_{\Upsilon_k}\}$. A proper Υ is then indicated by the minimum value in the set, given by

$$\Upsilon = \underset{\Upsilon_j}{\text{argmin}}(\{P_{\Upsilon_1}, P_{\Upsilon_2}, \cdots, P_{\Upsilon_k}\}), \quad j = 1, 2, \cdots, k \tag{7}$$

The reason for seeking the minimum probability peak is that a smaller probability peak always contributes to a smoother distribution (as shown by the red distribution in Figure 4). In this regard, more choices of spatial predictor selection are available, thus the preselection can be implemented more effectively.

The optimized time shift for each selected spatial predictor is located where the correlation coefficient reaches the maximum, given by

$$\bar{\gamma}_i = \underset{\delta t}{\text{argmax}}(\rho_{i,\delta t}), \quad i \in \overline{\Phi} \tag{8}$$

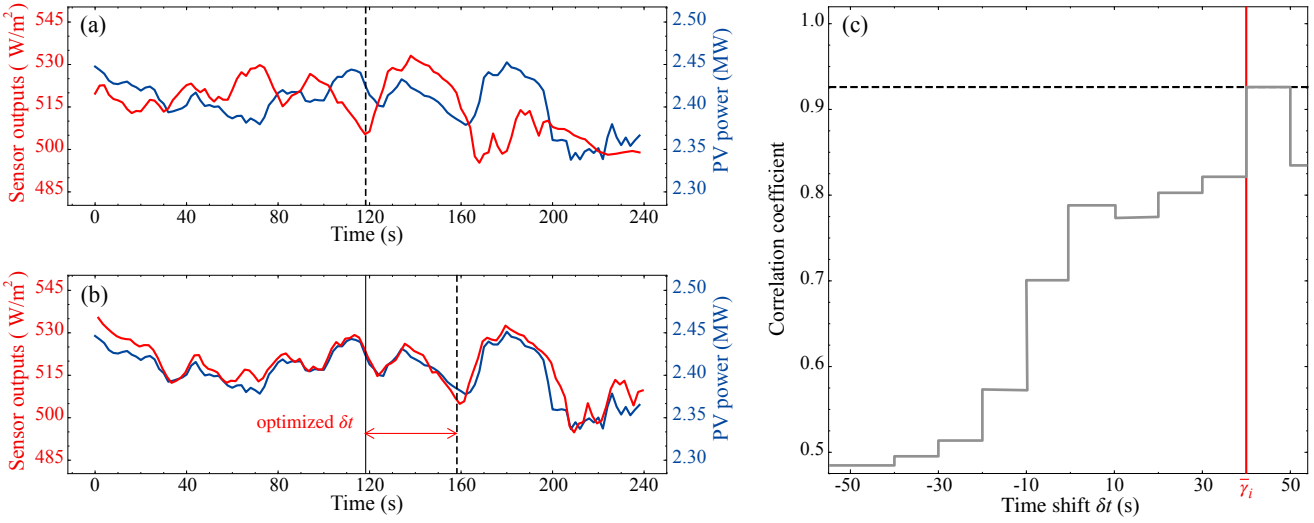

Figure 5: An example of seeking the optimized time shift between an individual sensor and focal PV system in a stationary scenario, with $\Upsilon = 0.8$, $h = 10$ s, $n = 5$ over an observation window T_{obs} 240 s. (a) The original time series of sensor measurements (red line) and focal system outputs (blue line). (b) The sensor measurement series is shifted with an optimized δt. (c) The correlation plot in regard to an increasing δt, and the optimized time shift $\bar{\gamma}_i$ is found as 40 s ($\bar{n}_t = 4$), when the correlation coefficient reaches the maximum, 0.927.

The number of temporal predictors, $\bar{n}_t$ is then indicated by the largest $\overline{\gamma}_i$,

$$\bar{n}_t = \frac{\max(\overline{\gamma}_i)}{h}, \quad i \in \overline{\Phi} \tag{9}$$

An example of seeking the optimized time shift for an individual sensor is illustrated in Figure 5, and the procedures will be conducted for all the sensors simultaneously.

Finally, the preselected stationary ST predictors can be formulated as

$$\bar{\mathbf{x}}(i;\bar{n}_t) = \Big[\underbrace{\bar{x}_{i,t-h} \quad \bar{x}_{i,t-2h} \quad \cdots \quad \bar{x}_{i,t-\bar{n}_t h}}_{\bar{n}_t}\Big], \; i \in \overline{\Phi} \tag{10}$$

where $\bar{\mathbf{x}}(i;\bar{n}_t) \in \mathbb{R}^{1\times(\bar{n}_s\times\bar{n}_t)}$.

3.2.2. Preselection in ramp scenarios

In ramp scenarios, CSV becomes the vital determinant for ST predictor preselection. Two factors, namely cloud shadow size and cloud shadow velocity affect the spatial and temporal correlations among the sensors respectively. On one hand, the unshaded sensors under different CSV coverage sizes can introduce irrelevant spatial predictors. On the other hand, various cloud shadow velocities can rise changeable time lags between the sensor measurements and focal system. As a result, a faster preselection algorithm capable of capturing CSV dynamics is demanded. At this stage, the peak difference minimization (PDM) algorithm is proposed, which allows an online CSV tracking and adaptive updates of ST predictors.

The basic principle of PDM is that the frequent cloud coverage and opening in ramp scenarios will show negative and positive peaks in sensor readings, and influence the exterior and interior sensors sequentially. Once the sensors with similar peaks are matched, the corresponding time lag between the sensor readings is available, and the CSV can be derived. Notice that an assumption has been made that the CSV remains approximately unchanged during the transit. Typically, CSV velocities can reach tens m/s [33], and the transit time for a CSV passing through the network may merely last for few minutes. It is therefore reasonable to consider that the assumption can hold within such a short time period.

Algorithm 1 shows the implementation of PDM. A trigger signal is first defined to control the activation of the algorithm, initialized to zero. When an exterior sensor $i \in \Phi^{ext}$ is first observed to experience a sudden value change $\Delta\tilde{x}_{i,t_0}$ at time instant t_0, the trigger signal will be set to 1, and PDM will be activated to estimate a time buffer Δt to support GFC. In this sense, a CSV has to be computed before $t_0 + \Delta t$ (the estimation of Δt varies with different CSVs and GFC regulations). Then PDM will keep tracking other value changes among the rest of sensors. Within the predefined time interval, PDM tries to identify as many sensor value changes as possible, and all the recorded sensors are appended to a new set $\widetilde{\Phi}$, implicating the selected spatial predictors. As a result, only the sensors with sudden value changes (the shaded sensors) are considered as spatial predictors, and the unshaded sensors can be excluded.

Algorithm 1 Peak Difference Minimization

Input: Sensor set: Φ, Φ^{ext} and Φ^{int}, Sensor sampling time: T_s, Error tolerance: ϵ, Alignments of sensor pairs: $\vec{d}_{i,j}$.
Output: Spatial predictor set: $\widetilde{\Phi}$, Global CSV: $\vec{V}$.

initial $\widetilde{\Phi} = \{\varnothing\}$, $trigger = 0$, $\delta t = 0$;
for $i \in \Phi^{ext}$ **do**
  Record the first sudden sensor reading change, $\Delta\tilde{x}^i_{t_0}$;
  $trigger = 1$;
  Estimate the required time buffer for GFC, Δt;
  Append sensor i to $\widetilde{\Phi}$;
end for
if $trigger == 1$ **then**
  while $t < t_0 + \Delta t$ **do**
    for $j \in \{\Phi - \widetilde{\Phi}\}$ **do**
      Record another sudden reading change, $\Delta\tilde{x}^j_t$;
      Append sensor j to $\widetilde{\Phi}$;
      for $\delta t = 0; \delta t \le t_0 + \Delta t - t; \delta t \mathrel{+}= T_s$ **do**
        $\tau_{i,j} = \underset{\delta t}{\operatorname{argmin}}(|\Delta\tilde{x}_{i,t_0} - \Delta\tilde{x}_{j,t_0+\delta t}| < \epsilon)$;
      end for
    end for
  end while
end if
if $\widetilde{\Phi} \cap \Phi^{int} \neq \{\varnothing\}$ **then**
  for $j \in \{\widetilde{\Phi} - i\}$ **do**
    $\vec{V} = \sum \frac{\vec{d}_{i,j}}{\tau_{i,j}}$;
  end for
  return $\widetilde{\Phi}, \vec{V}$;
end if

To determine the peak sameness, instead of comparing the peak values directly, PDM checks how close the value changes are. The biggest advantage of comparing the value changes is that the differencing can eliminate the inherent sensor calibration errors. A small positive value ϵ is then applied as an error tolerance to control the confidence level of peak sameness. With an increasing time shift δt, two sensors i, j are said to be correlated at $\tau_{i,j}$ once the difference between their value changes is smaller than ϵ. Together with the known spatial distance $\vec{d}_{i,j}$, the global CSV, $\vec{V}$ is obtained. Notice that only when the intersection of set $\widetilde{\Phi}$ and set Φ^{int} is not empty would PDM output the results. In another word, the CSV should cover at least one interior sensor. In case of a CSV that only covers exterior sensors, it is deemed to cause no impact on the focal PV system, thus there is no need for preselection.

Then the time lag between the selected sensors and focal PV system can be estimated by

$$\tilde{\gamma}_i = \frac{\vec{D}_i}{\vec{V}}, \quad i \in \widetilde{\Phi} \tag{11}$$

where $\vec{D}_i$ is the spatial distance between the sensor i and the focal PV system. The number of temporal predictors

is determined by the largest $\widetilde{\gamma}_i$,

$$\widetilde{n}_t = \max(\frac{\widetilde{\gamma}_i}{\Delta t}), \quad i \in \widetilde{\Phi} \tag{12}$$

Finally, the preselected ramp ST predictors can be formulated as

$$\tilde{\mathbf{x}}(i;\tilde{n}_t) = \Big[\underbrace{\tilde{x}_{i,t-T_s} \;\; \tilde{x}_{i,t-2T_s} \;\; \cdots \;\; \tilde{x}_{i,t-\widetilde{n}_t T_s}}_{\widetilde{n}_t}\Big], \; i \in \widetilde{\Phi} \tag{13}$$

where $\tilde{\mathbf{x}}(i;\tilde{n}_t) \in \mathbb{R}^{1\times(\tilde{n}_s\times\tilde{n}_t)}$, and $\tilde{n}_s = \mathrm{card}(\widetilde{\Phi})$ indicates the number of selected spatial predictors.

3.2.3. A complete preselection function

At this stage, a complete ST preselection mechanism is developed, and the following functions should apply:

$$\begin{cases} n_s = \mathrm{sel}(\mathrm{card}(\Phi), \mathrm{card}(\widetilde{\Phi}), \zeta_t) \\ n_t = \max\big(\mathrm{sel}(\frac{\overline{\gamma}_i}{\Delta t}, \frac{\widetilde{\gamma}_i}{\Delta t}, \zeta_t)\big) \end{cases} \tag{14}$$

and

$$\mathbf{x}(i;n_t) = \Big[x_{i,t-t_s} \; x_{i,t-2t_s} \cdots x_{i,t-n_t t_s}\Big], \quad i \in \mathrm{sel}(\Phi, \widetilde{\Phi}, \zeta_t) \tag{15}$$

where $\mathrm{sel}(a,b,\zeta_t)$ is the selection function, which outputs a when $\zeta_t = 0$ (stationary scenarios), and outputs b when $\zeta_t = 1$ (ramp scenarios). In this way, different ST prediction preselection strategies can be automatically applied based on the scenario recognition signal.

Notice that although the use of the largest time lag $\widetilde{\gamma}_i$ in (9) and (12) may result in irrelevant temporal predictors included in the model, the computational complexity is greatly reduced. This problem will be further addressed in Section 3.3, where a penalized model is introduced for additional predictor filtering.

3.3. PV Nowcasting Strategy

Prior to PV nowcasting, the GHI data from the sensor network are transformed into clear-sky index data in order to remove diurnal patterns in the GHI time series. Such transformation is often referred as detrending. Given a sensor i at time t, the detrending is defined as

$$k^*_{i,t} = \frac{x_{i,t}}{x^{clr}_{i,t}} \tag{16}$$

where $k^*_{i,t}$ is the clear-sky index, $x_{i,t}$ and $x^{clr}_{i,t}$ denote the measured GHI and clear-sky irradiance respectively. In this work, the clear-sky irradiance for each sensor or focal PV system is generated directly by fitting the measured data on a clear day in the most recent past, as introduced in [34]. After prediction, the nowcasted clear-sky indices are converted back to GHI or PV power. The advantage of using this data-driven method for clear-sky index generation rather than applying a clear-sky model is that the real data can inherently account for the measurement discrepancies such as orientations and calibration errors.

3.3.1. Nowcasting model

As mentioned earlier, the preselection in both scenarios may introduce irrelevant temporal predictors. To address this problem, a penalized regression model becomes useful to provide further predictor filtering. The ridge regression and lasso are two frequently used penalized regression models. The former penalizes the residual sum of squares using an ℓ_2-penalty, while the latter takes ℓ_1-penalty. The biggest advantage of ridge regression is its stability and strong tolerance to small changes in model inputs. However, the ridge regression estimates always retain a whole set of predictors. In contrast, lasso can completely exclude the unexpected predictors from the model by shrinking their parameters to zero. However, lasso may lose its effectiveness when strong collinearity or aggregation effect is observed among the predictors, which is just the case for the sensors under a same cloud coverage. Consequently, only few or even one predictor is selected, and the model become less interpretable. In this work, we introduce the elastic-net, whose regularization term is a convex combination of ℓ_1-penalty and ℓ_2-penalty. The integration of both ℓ_1 and ℓ_2 penalties allows for leaning a sparse model with fewer zero weights than lasso, while maintaining the stability as ridge regression.

Given a data set with n predictors and m samples $X \in \mathbb{R}^{m\times n}$, and responses $Y \in \mathbb{R}^{m\times 1}$, the elastic-net estimator is given by

$$\hat{\Theta} = \underset{\Theta}{\mathrm{argmin}}\left\{ \|X\Theta - Y\|_2^2 + \lambda\alpha\|\Theta\|_1 + \lambda(1-\alpha)\|\Theta\|_2^2 \right\} \tag{17}$$

where $\Theta \in \mathbb{R}^{n\times 1}$ is the regression parameter, and $\lambda > 0$ is the regularization parameter which regulates the strength of the penalty. The larger the value of regularization parameter λ, the greater the amount of shrinkage and thus the parameters become more robust to collinearity. Specially, the elastic net transforms into ridge regression when $\alpha = 0$, and becomes lasso when $\alpha = 1$. In this work, all the parameters are selected using the k-fold cross validation.

3.3.2. Coordinated nowcasts

As aforementioned, a fixed prediction horizon h is available in the stationary scenarios. However, the prediction horizon in ramp scenarios, $\widetilde{n}_t T_s$ is limited by the size of the network and CSV velocities. The larger the CSV velocity and the smaller the network dimensions, the shorter prediction is provided. To aggregate the predictions in two scenarios, a coordinated framework is developed, as shown in Figure 6.

In the stationary scenarios, the ST correlations among the sensors present to be more stable due to the steady irradiance resources. In this sense, the stationary predictor set $\bar{\mathbf{x}}(i;\bar{n}_t)$ is only updated for each time interval ΔT to adapt the gradual attributes change, e.g. ambient temperature, pressure and humidity, etc. In the ramp scenarios, beside updating the ramp predictor set $\tilde{\mathbf{x}}(i;\tilde{n}_t)$, the latest

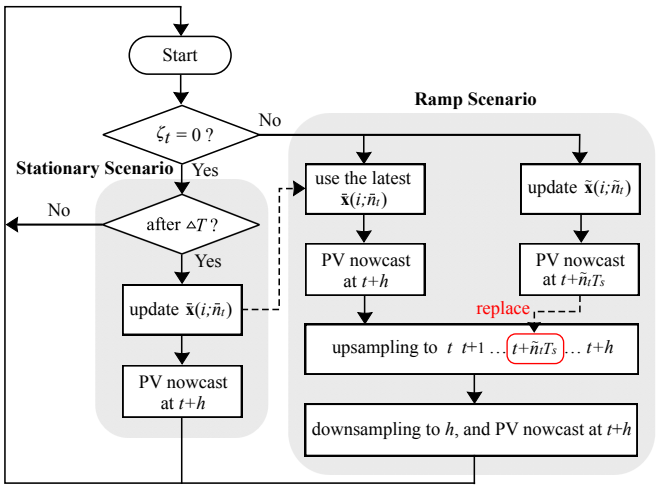

Figure 6: Flowchart of the developed coordinated nowcasting. The consistent PV nowcasts with a fixed prediction horizon at $t+h$ is available in stationary scenarios. The forecasts are then further complemented when the CSV is detected at $t+\tilde{n}_t T_s$ in ramp scenarios.

preselected stationary predictors is also used for consistent PV nowcasting at $t+h$. Then the $t+h$ nowcast with resolution of h is upsampled to the 1-s sequence, with backward interpolation. When the CSV is detected, the interpolated value at $t+\tilde{n}_t T_s$ will be replaced by the nowcasting result. The value sequence is then downsampled back to h by calculating the mean of the sequence. In this way, consistent PV nowcasts with a fixed prediction horizon of h becomes available in both of the scenarios, while the cloud dynamics is contained.

4. Results

In this section, a concentric network prototype with 5 sensors is deployed on the rooftops, whose layout is shown in Figure 7. The network consists of 3 exterior sensors $\Phi^{ext} = \{S_2, S_3, S_4\}$, and 2 interior sensors $\Phi^{int} = \{S_1, S_5\}$. Another sensor is used to mimic the generation of a 5 MW

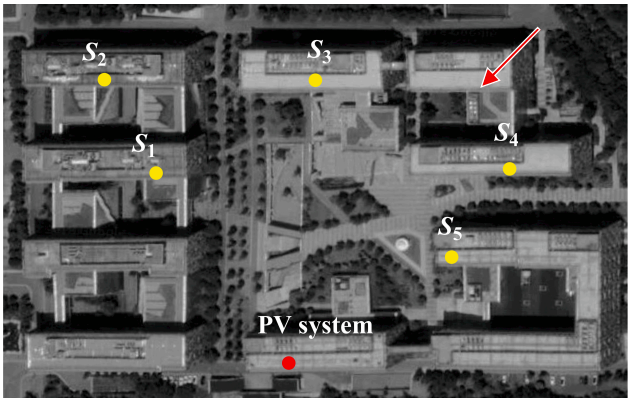

Figure 7: Layout of the deployed sensor network prototype, with 3 exterior sensors and 2 interior sensors. Arrow in the top shows the dominate wind direction.

PV system. Refer to the design in Figure 2, the specific network deployment is displayed in Table 1. The central server is equipped with Intel Core i7 2.9-GHz CPU. All the processing is carried out using Python. The system is operated continuously from November 1, 2018 to April 1, 2019. Due to the limited experimental configuration, only the data measured in the days with dominated wind directions from 0° to 60° north is used. After several calibration tests, the correlation coefficient threshold is found as $\Upsilon = 0.8$, the threshold value for scenario recognition is chosen to be $P_{th} = 2.5$, and the error tolerance of PDM is set as $\epsilon = 5$.

4.1. Error metrics

To evaluate the proposed nowcasting strategy, several error metrics are used in this work. Given the measured PV generation y_i, and the predicted value $\hat{y}_i$, the normalized root mean square error is given by

$$\text{nRMSE} = \frac{\sqrt{\frac{1}{m}\sum_{i=1}^{m}(y_i - \hat{y}_i)^2}}{\frac{1}{m}\sum_{i=1}^{m} y_i} \times 100\% \qquad (18)$$

The forecast skill proposed in [35] is given by

$$\text{FS} = 1 - \frac{\text{nRMSE}}{\text{nRMSE}_p} \qquad (19)$$

where nRMSE_p is the nRMSE produced by the persistence model. The metric FS equals to 1 for a perfect forecast, and takes a negative value when the proposed model is inferior to the persistence model.

For GFC application such as ramp-rate control, forecasts of peak values (both positive and negative) during each ramp event become critical [36]. In this regards, the normalized peak mean absolute error (nPMAE) is proposed, given by

$$\text{nPMAE} = \frac{\frac{1}{m_p}\sum_{i=1}^{m_p} |y_i^p - \hat{y}_i^p|}{\frac{1}{m_p}\sum_{i=1}^{m_p} y_i^p} \times 100\% \qquad (20)$$

where m_p is the number of peaks, y_i^p and $\hat{y}_i^p$ denote the measured and predicted peak values respectively. The nPMAE also measures the model adaptability to the CSV.

Table 1: Spatial distances in meters (m) between the sensors. The maximum distance is found as 224 m between S_2 and S_4. The minimum distance is found as 55 m between S_4 and S_5.

	S_1	S_2	S_3	S_4	S_5	PV
S_1	-	58	100	193	168	130
S_2	58	-	116	**224**	200	185
S_3	100	116	-	116	122	152
S_4	193	**224**	116	-	**55**	158
S_5	168	200	122	**55**	-	100

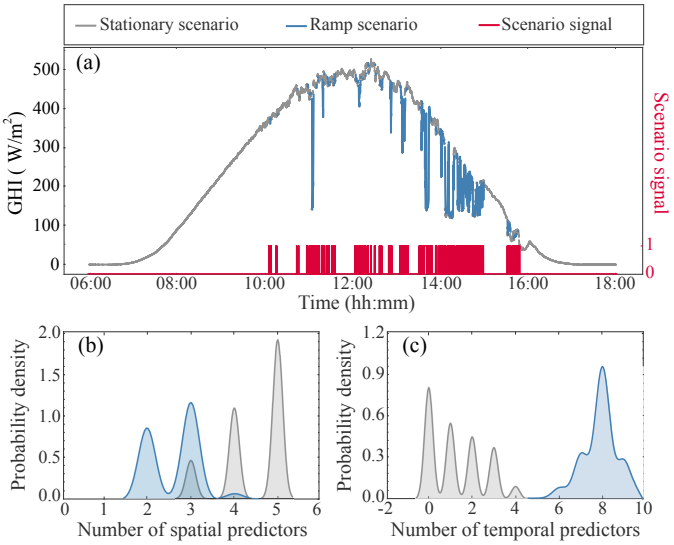

Figure 8: The preselection example for a moderate day on 2018 December 24. (a) PV generation profiles and scenario recognition results, where the grey line and blue line represent the recognized stationary and ramp scenarios respectively, and the red line shows the scenario signal. (b) Results of spatial predictor preselection using SRP. (c) Results of temporal predictor preselection using SRP.

4.2. Results of predictor preselection using SRP

To demonstrate the effect of SRP preselection, we consider a preselection example on a day with moderate variability, on 2018 December 24. In this example, consistent PV nowcasts with a prediction horizon $h = 10$ s are generated. Thus the data processed in stationary scenarios are averaged into 10-s intervals. In addition, a fixed GFC time buffer for PDM is chosen as $\Delta t = 5$ s, and the stationary predictors is set to be updated for each $\Delta T = 10$ min.

Before implementing SRP, the scenario recognition signal is generated to describe the real-time PV dynamics, as shown in Figure 8(a). In this case, 13% data points are identified as ramp. Figure. 8(b) and Fig. 8(c) show the spatial and temporal preselection results respectively. It can be seen that 5 spatial predictors, that is, a whole set of sensors are mostly selected in the stationary scenarios, and at least 3 spatial predictors are included. This indicates that strong spatial correlations can be observed among the sensors during these periods. In the ramp scenarios, fewer spatial predictors are selected. Except for the two necessary along-wind sensors, the PDM typically preselects one additional spatial predictor, and maximum two are preselected (in very few cases). The selection is mainly limited by the predefined GFC time buffer, which is fixed as 5 s in this case. The effect of varying Δt will be further studied in Section 4.4.

For the temporal predictor preselection, it can be seen that only few or even no temporal predictor is selected in the stationary scenarios (0 in most cases). This is mainly due to the steady irradiance received during these periods, which greatly relieves the solar temporal dynamics. In the ramp scenarios, 8 predictors are mostly selected, implicating a time lag of 8 s. Considering an average distance of 56.5 m between the focal system and interior sensors (S_4 and S_5), the average detected CSV velocity is estimated as 7 m/s. Notice that the actual wind speed during the day has been reported as 6.5 m/s, which proves the proposed SRP method to be effective to track CSV.

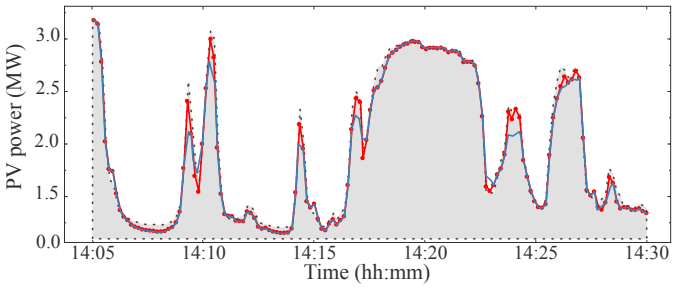

Figure 9: Nowcasting using SRP (red line) and measured PV generation (black dotted line) for a period on 2018 December 24. Nowcasting results before coordination (using stationary predictors only) is represented by the blue solid line. After coordination, the predictions approach closer to the actual peaks.

4.3. Results of coordinated PV nowcasts

Once the ST predictors are preselected, the 10-s ahead nowcasting is generated by coordinating the results in the two scenarios. For each prediction, only the adjacent 720 data points (approximately 20% data of the whole day) are used for training, implicating the most recent 120 and 12 minutes data respectively for stationary and ramp scenarios. For a single nowcast, the computation time can be controlled within 10 ms, which makes the proposed method feasible for real-time GFC.

To visualize the coordination effects, a snapshot from 14:05 to 14:30 is plotted in Figure 9. It can be seen that the coordination improves the nowcasts significantly. Before coordination, only stationary predictors are fed into the model, thus it performs better when less fluctuations are observed. For the nowcasts during large ramps, the performance deteriorates as the predicted values always fail to reach the ramp peaks. After coordination, the ramp predictors begin to enter the model, making it more adaptive to the fast moving CSVs. In this way, the nowcasts generated by stationary predictors are further complemented, with the predicted values approaching closer to the ramp peaks. During this specific time period, the nPMAE before coordination is found as 15.80%, and reduces to 8.47% (43.4% improvements) after coordination. For the nowcasts of the entire day, the nRMSE, FS, and nPMAE are 4.71%, 0.40, 7.98% respectively.

4.4. Case study 1: nowcasting under various GFC time buffers

The previous example assumes a fixed GFC time buffer. In practice, however, the required time buffer can vary from case to case according to different GFC regulations. Therefore, we investigate the effect of various GFC time

Table 2: The nowcasting performance for various GFC time buffers. 30-s ahead nowcasting is generated on 2018 December 24.

Δt (s)	nRMSE (%)	nPMAE (%)	FS
2	5.05	10.56	0.36
5	4.71	7.98	0.40
10	**4.64**	**7.07**	**0.41**
20	5.35	12.05	0.32
30	5.68	16.87	0.27
60	5.68	16.87	0.27

buffers on nowcasting accuracy in this case study. Recall the coordination flowchart in Figure 6, the ramp predictor set ought to be updated before time $t+h$, implicating $\Delta t < h$. Otherwise the prediction becomes useless. In this sense, we consider herein the 30-s ahead nowcasting to provide more choices of Δt. The results are depicted in Table 2.

It can be seen that the accuracy reduction with different time buffers is marginal. The use of 5-s and 10-s time buffers generate comparable results, and outperform the other cases. This result aligns with the discussions in Section 4.2. With an average wind velocity of 6.5 m/s, it generally takes 8 s for a CSV to arrive the focal PV system. Thus to effectively preselect the relevant predictors in a ramp scenario, a searching time near 8 s is preferred. However, for most GFC applications, the CSV has to be identified before it reaches the focal system. In this regard, the 5-s choice seems to be superior to the 10-s case although the 10-s time buffer offers slight improvements.

It is also found that when $\Delta t > 10$ s, the performance begin to deteriorate. This is due to the slow preselection process that may not be able to timely update the ramp predictors. For the case of $\Delta t = 20$ s, there is only a 10-s interval before generating nowcasts (since the ramp predictors should be updated before $t + 30$ s). Consequently, only the CSVs occurred between t and $t+10$ can be identified. As Δt further increases, eventually there would be no CSV being reported (such as the 30-s and 60-s cases). As a result, only stationary predictors are fed into the model, and the model becomes less robust in ramp scenarios with larger nPMAE errors. On the other hand, when the time buffer is insufficient (such as the 2 s case), fewer predictors are preselected, which also hinders the nowcasting performance.

4.5. Case study 2: nowcasting using various training data lengths

In this case study, we evaluate the effect of training data length on the nowcasting performance. The 10-s ahead nowcasts are generated as the previous example. In addition, another 9 cloudy days with similar wind directions are selected for generalization (totally 10 days). To benchmark the proposed method, the persistence (Pers), linear regression (LR), and long short-term memory recurrent neural networks (LSTM) models are used.

Table 3: The 10-s ahead nowcasting performance of the proposed method (SRP-Enet) and benchmarking models for various training data points. The results are averaged over the 10 days.

Length		Pers	LR	LSTM	SRP-Enet
360	nRMSE (%)	8.24	8.82	9.92	6.57
	nPMAE (%)	18.20	19.96	14.70	12.67
	FS	-	-0.07	-0.20	0.20
720	nRMSE (%)	8.24	6.74	8.34	**5.83**
	nPMAE (%)	18.20	15.92	14.61	**8.57**
	FS	-	0.18	-0.01	**0.29**
1080	nRMSE (%)	8.24	6.70	8.19	6.18
	nPMAE (%)	18.20	15.21	14.37	10.42
	FS	-	0.19	0.01	0.25
1440	nRMSE (%)	8.24	6.63	7.91	6.29
	nPMAE (%)	18.20	14.90	14.08	11.24
	FS	-	0.20	0.04	0.24
1800	nRMSE (%)	8.24	**6.58**	**7.64**	6.37
	nPMAE (%)	18.20	**14.62**	**13.97**	11.78
	FS	-	**0.20**	**0.07**	0.23

The Pers model is the most commonly used and simplest type of solar nowcasting. It assumes the conditions (irradiance, temperature, cloud coverage, etc.) remain the same between t and $t+h$. Thus the Pers model only shows promising results at very short time horizons, making it a standard for benchmarking solar nowcasting [37, 38]. The LR is also a commonly used benchmark model for ST nowcasting. When a short prediction horizon is desired, the strong linearity between the measurements of sensors and focal PV system makes the regression based model a priority for solar nowcasting [22, 39]. Furthermore, in order to compare with the recent advances in AI-enhanced technology, the LSTM model, which is typically applied to time-series forecasting, is included for comparison as well [40].

The LSTM model used here is constructed with 50 neurons in the first hidden layer and 1 neuron in the output layer for prediction. The model is fit for 50 epochs with a batch size of 10. The LR and LSTM models use the same training data length as the proposed method. In addition, the CSV information is unknown to the two models, thus sufficient ST predictors are assumed, i.e. a whole set of 5 spatial predictors and 10 temporal predictors. The persistence model directly transforms the measurements of sensor S_5 to PV generation. The results are displayed in Table 3.

It is an interesting finding that the proposed SRP-Enet method generates the best nowcasts with 720 data points (20% training length). As the training data length further increases, its performance deteriorates instead. This is mainly due to the effects of SRP, where the predictors are constantly updated. As a result, data collected several hours ago may not be suitable to fit the latest preselected predictors. For LR and LSTM models, their accuracies decrease when the training data become fewer. Even when the data is sufficient such as using 1800 points (data col-

lected within 5 hours, accounting for 40% of the whole data set), due to the large number of irrelevant predictors, their performances are still inferior to that of of the SRP-Enet. Furthermore, it can be seen that the more advanced LSTM model is beaten even by a simple LR model in the tests. This observation is consistent with the discussions in [22] that the strong correlations among the predictors makes the regression-based methods a priority for PV nowcasting application.

We note that the problem of training data length may be relaxed for practical operation by using the historical data in similar meteorological conditions. In this regard, the performance of LSTM-type models may be further improved. However, this case study verifies that the proposed method can use much fewer training data while achieving similar or better results than the other models, which makes the proposed method more advantageous when historical data becomes unavailable.

4.6. Case study 3: nowcasting with various prediction horizons

In the previous studies, performance of the SRP-Enet along with several benchmarking models is evaluated at a prediction horizon of 10 s. In this case study, nowcasts with various prediction horizons are presented. Data from the selected 10 days are averaged into 10, 20, 30, 60, and 300 s intervals. Based on the results from case study 2, the most recent 20% data are used for training. Table 4 shows the nowcasting results.

It can be concluded from Table 4 that the proposed SRP-Enet method has a better performance than the benchmarking models for all the prediction horizons. For the prediction within 60 s, cloud dynamics still dominates the accuracy, thus the inclusion of temporal predictors in the model can significantly improve the nowcasts. For h = 300 s, the impacts of CSV is greatly relieved thanks to the well-known temporal smoothing effect [41]. In this case, the inclusion of unnecessary temporal predictors is likely to deteriorate the nowcasts, which accounts for the unacceptable results of the LR model. Although the redundant temporal predictors are also included in the SRP-Enet, the inherent regularized term of elastic-net model provides a supplementary predictor filtering. Thus the SRP-Enet is still comparable to the persistence model. It is also observed that as the prediction horizon expands, the nPMAE differences between the models decreases rapidly. This also verifies the temporal smoothing effect at larger prediction horizons.

Table 4: Nowcasting performance of the proposed SRP-Enet and benchmarking models at various prediction horizons. The results are averaged over the 10 days.

h (s)		Pers	LR	LSTM	SRP-Enet
10	nRMSE (%)	8.24	6.74	8.34	5.83
	nPMAE (%)	18.20	15.92	14.61	8.57
	FS	-	0.18	-0.01	0.29
20	nRMSE (%)	7.84	6.00	7.33	4.86
	nPMAE (%)	15.34	12.58	13.22	7.26
	FS	-	0.23	0.06	0.35
30	nRMSE (%)	6.91	5.67	6.84	4.59
	nPMAE (%)	10.59	9.53	10.07	6.88
	FS	-	0.18	0.01	0.34
60	nRMSE (%)	5.53	4.92	5.37	4.24
	nPMAE (%)	8.28	7.82	8.15	6.32
	FS	-	0.11	0.03	0.23
300	nRMSE (%)	2.35	4.02	2.59	2.30
	nPMAE (%)	4.50	7.08	5.11	3.95
	FS	-	-0.7	-0.1	0.02

4.7. Case study 4: nowcasting in different weathers

So far the studies have shown that the proposed SRP-Enet model is able to produce better results in cloudy days. In this case study, we investigate the nowcasting performance in different weathers, namely, the sunny, cloudy, and rainy days. For each weather type, 10 days are selected during the experimental days. Based on the previous studies, 20% data are used for training to generate 10-s ahead PV nowcasts. Figure 10 shows the examples of nowcasting in the 3 typical weather conditions.

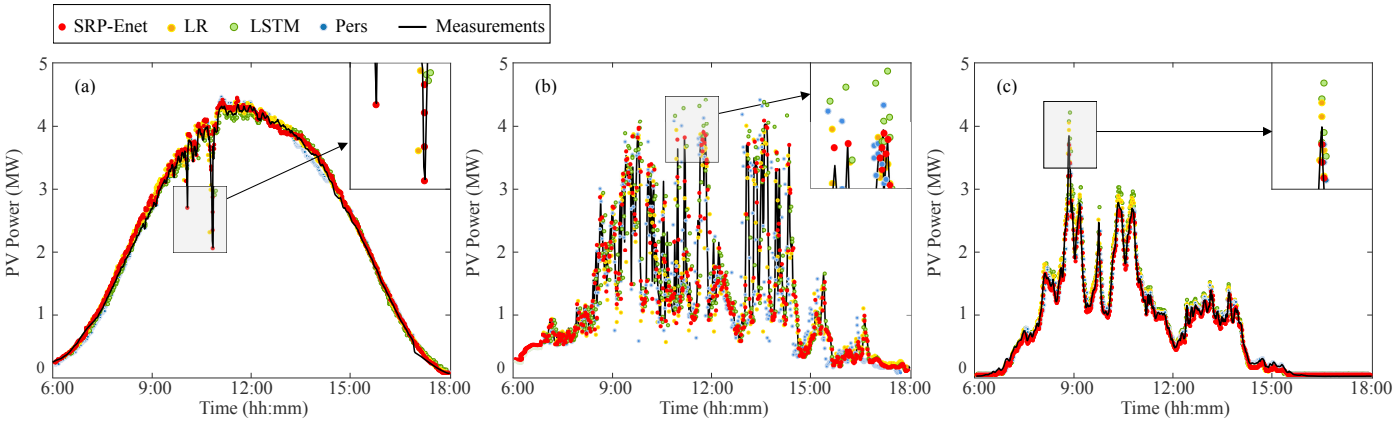

Figure 10: Nowcasting examples under typical weather conditions (a) sunny, (b) cloudy, (c) rainy. The proposed SRP-Enet method approaches the closest to the ramp peaks compared with the other methods.

It can be seen from Figure 10 that the SRP-Enet nowcasts approach close proximity to the ramp peaks in all weather conditions, which is otherwise unachievable using other methods. This property should become especially important for GFC application such as ramp-rate control, where the peak values dominate the control operations. Table 5 depicts the nowcasting performance during the respective 10 days. It is evident from Table 5 that the SRP-Enet method generally outperforms the benchmarking methods in all weathers, with an apparent reduction in term of nPMAE. In the cloudy days, the SRP-Enet nowcasts show an average nRMSE and nPMAE improvements over 13.5% and 41.3% compared with the benchmarking methods. At first glance the SRP-Enet does not show as much nRMSE improvements in sunny days as it does in cloudy days. Due to the infrequent cloud coverages in the sunny days, even a large error of predicting PV fluctuations may not significantly influence the nRMSE. In this regard, the nRMSE is unfaithful to tell the reliability of the nowcasts. On the contrary, the nPMAE, which aims to describe the ability of predicting PV ramps, becomes useful. In the sunny days, the nPMAE improvements by the SRP-Enet is more than 20% over the other methods. Another observation can be made is that the SRP-Enet nowcasts in the rainy days present to be inferior to the persistence model in term of nRMSE. As the CSV diminishes in precipitation, the raining periods are always referred to the stationary scenarios. However, the meteorological features such as ambient temperature and humidity can change rapidly during these periods. Thus a interval of $\Delta T = 10$ min for updating stationary predictors may not response to these sudden changes in time.

We have noticed that in some areas, additional weather types such as snowstorm and sandstorm may also be observed. In these cases, however, the proposed SRP-Enet forecasting can still be utilizable, since the sensors can feel the snow drop or sand cover as similar as the PV system is experiencing (the sensor material, tilt angle etc. are similar to the focal PV system).

Table 5: Nowcasting performance in different weather conditions. 10 typical days are selected for each weather type. The results are averaged over the respective days.

		Pers	LR	LSTM	SRP-Enet
Sunny	nRMSE (%)	2.71	2.37	3.19	**2.35**
	nPMAE (%)	6.64	5.98	7.02	**4.81**
	FS	-	0.13	-0.18	**0.13**
Cloudy	nRMSE (%)	8.24	6.74	8.34	**5.83**
	nPMAE (%)	18.20	15.92	14.61	**8.57**
	FS	-	0.18	-0.01	**0.29**
Rainy	nRMSE (%)	**4.59**	5.01	5.65	4.92
	nPMAE (%)	7.86	9.26	10.99	**7.17**
	FS	-	-0.09	-0.23	**-0.07**

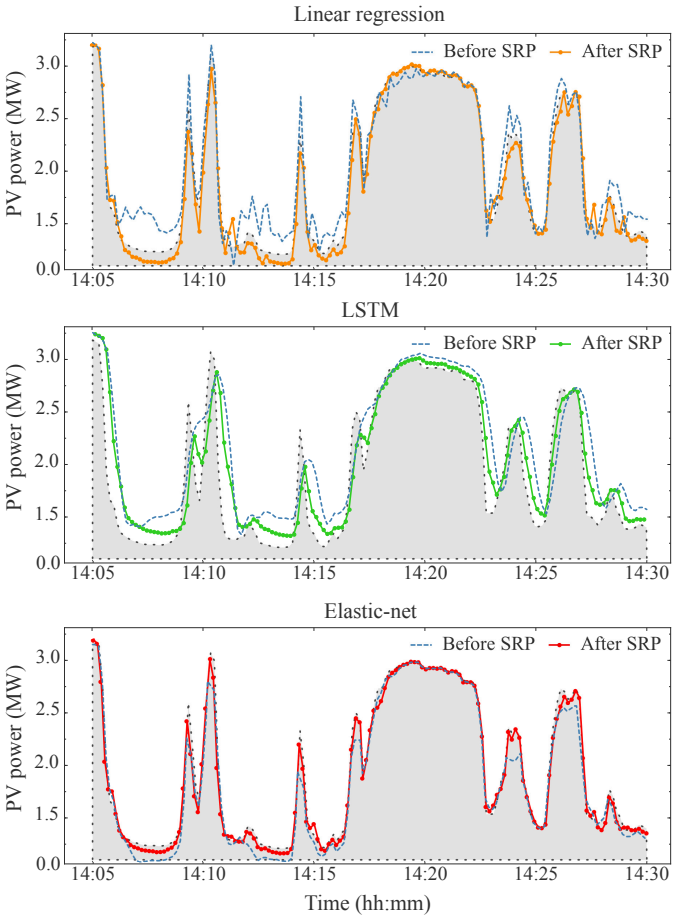

Figure 11: Nowcasts before and after applying SRP to all the models for a period on 2018 December 24. The measured PV generation is represented by the black dotted line. **Top,** linear regression. **Middle,** LSTM. **Bottom,** elastic-net.

4.8. Case study 5: applying SRP to all the models

The last case study in this paper evaluates the effects of SRP. Nowcasts with and without the favor of SRP are studied for all the models. When SRP is unavailable, sufficient ST predictors, i.e., a full set of spatial predictors $n_s = 5$ with temporal lag $n_t = 10$, are considered. The configurations of this case study are identical to case study 4, namely, generating 10-s ahead nowcasts with a training length of 20%. The results are generalized on the 10 cloudy days to exclude the non-cloud factors (such as the sudden change of temperature and humidity in rainy days). Figure 11 shows the snapshots of nowcasts using different models before and after applying SRP.

Before SRP, a large number of irrelevant predictors are fed to the models. Consequently, the LR nowcasts typically become much more fluctuated than expected (see the top plot), and the LSTM nowcasts present to be lagging to the measurements (see the middle plot). Benefiting from its penalty term, the elastic-net produces much more smooth nowcasts than LR, and there is no lag between the predicted and measured time series (see the bottom plot). However, it is still far beyond satisfactory since it

Table 6: Nowcasting performance before and after applying SRP. The results are averaged over the 10 days.

		LR	LSTM	Elastic-Net
Before	nRMSE (%)	6.74	8.34	6.18
	nPMAE (%)	15.92	14.61	10.36
	FS	0.18	-0.01	0.25
After	nRMSE (%)	**6.12**	**6.58**	**5.83**
	nPMAE (%)	**10.02**	**10.27**	**8.57**
	FS	**0.26**	**0.20**	**0.29**

always fails to reach the ramp peaks. After SRP, it can be seen that the nowcasts for all the models are significantly improved. With proper predictors preselected, the LR nowcasts become more stable. The lagging issue of LSTM is also relieved. More importantly, all the nowcasts approach closer to the ramp peaks.

The error metrics before and after applying SRP for the models are shown in Table 6. It is observed that although the benchmarking models use the similar predictors, their performances are still inferior to the elastic-net based nowcasts. This observation validates the effectiveness of the penalty term of the elastic-net model, which is able to provide additional predictor reduction. In this case, the nRMSE improvements after applying SRP are found as 9.19%, 21.1%, and 5.66% respectively for the LR, LSTM, and elastic-net model. The nPMAE improvements are found as 37.06%, 29.71%, and 17.28%, respectively.

5. A practical application: PV power ramp-rate control

In this section, we demonstrate a practical GFC application of the proposed SRP-Enet nowcasting: PV power ramp-rate control (PRRC).

5.1. Basic principle

At present, the PV power ramp-rates are mitigated either by integrating energy storage system or curtailing PV active power. The former strategy utilizes the energy storages to save or release energy when PV generation increases or decreases faster than the ramp-rate limit. Although the control can be effective, the high cost of energy storages is still hindering its practical application. The latter strategy complies with the ramp-rate requirement by suppressing the real-time PV generation, namely, controlling the system working point away from the maximum power point. However, its application is limited at the power ramp-up side, since no external devices can be used to compensate the ramp-down fluctuations. As a result, a novel control strategy so-called battery-less PRRC emerges, which utilizes the very short-term PV forecasting [42, 43]. The control principle is shown in Figure 12(a).

For ramp-up fluctuations, the control works similar to the conventional power curtailment method, where the ramps are directly smoothed on the inverter level by regulating the maximum power point of PV panels. For ramp-down fluctuations, the integration of PV nowcasting allows to predict the power drop time at t_a and the resultant output change ΔP. Given a predefined ramp-rate limit R_s and system rated power P_{rated}, the control time t_c can be found by

$$\frac{\Delta P}{(t_a - t_c)P_{rated}} = R_s \tag{21}$$

In this way, both ramp-up and ramp-down fluctuations can be smoothed by active power curtailment, and no energy storage system is required. However, the performance of battery-less PRRC highly relies on the accurate prediction of upcoming ramps, especially the ramp peak magnitudes. Control with perfect forecasts as seen in Figure 12(a) are typically not available in practice. In the case of the predicted ramp peak is smaller than fact, as seen in Figure 12(b), a smaller power change ΔP is reported, leading to a delayed control time t_c. As a result, it causes a ramp violation. In the case of the predicted ramp peak is larger than the fact, shown in Figure 12(c), a larger ΔP can result in an earlier control time t_c. Consequently, more energy is curtailed or wasted.

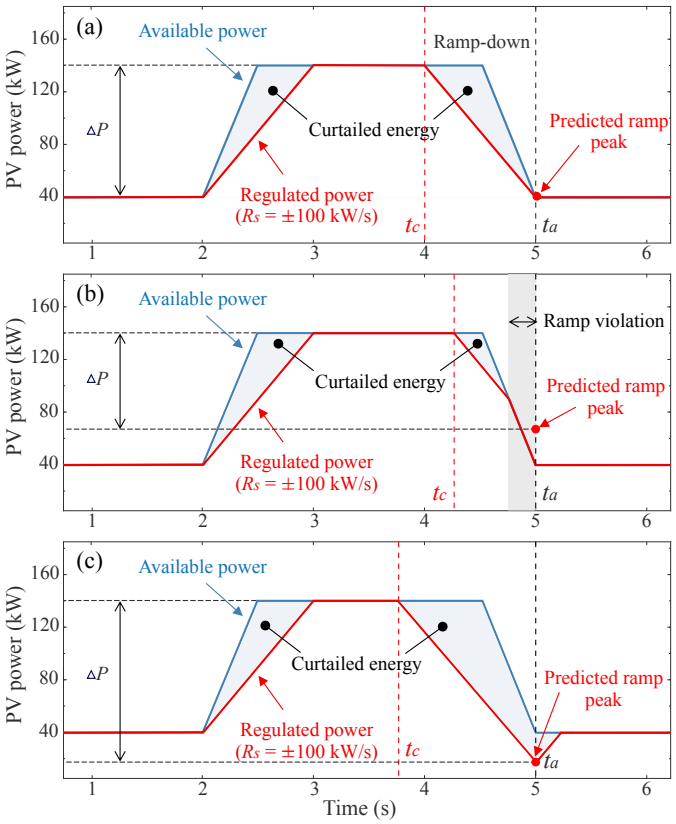

Figure 12: Implementation of battery-less PV power ramp-rate control. (a) Control with perfect forecast. The use of very short-term PV forecasting ensures power curtailment for both ramp-up and ramp-down fluctuations. (b) Control with inaccurate forecast. The predicted ramp peak is smaller than the fact, leading to a ramp violation. (c) Control with inaccurate forecast. The predicted ramp peak is larger than the fact, leading to more energy curtailment.

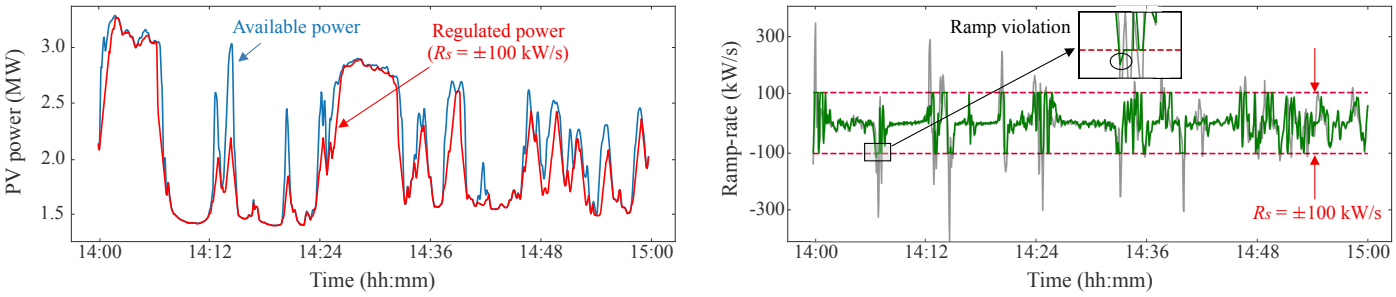

Figure 13: Results of the battery-less power ramp-rate control using 10-s ahead nowcasts for a period on 2018 December 24, with R_s= ±100 kW/s. **Left.** The original PV generation (blue line) and the regulated PV generation (red line). **Right.** The original ramp-rates (grey line) and regulated ramp-rates (green line). The ramp-rate limits are represented by the red dashed line.

To evaluate the performance of battery-less PRRC, the control failure and energy curtailment have been defined. The control failure is calculated as the ratio of the observed ramp violations over the total ramps during the target period. The energy curtailment is defined as the ratio of the curtailed energy over the total production during the target period.

5.2. Battery-less PRRC with SRP-Enet nowcasts

Before implementing the control, a ramp-rate limit R_s should be first defined. In this study, we follow the regulation in [5], where the maximum allowed ramp-rate is suggest to be 100 kW/s for the PV systems above 11 kW. It should be noticed that for battery-less PRRC application, the GFC time buffer Δt in PDM is no longer a fixed value. Given the first sensor reading change at t_0, the GFC time buffer equals to

$$\Delta t = t_c - t_0 \tag{22}$$

where t_c is the control time defined in (21), which changes with different CSVs. According to the previous case studies, the 10-s ahead PV nowcasts are generated with a training data length of 20%. The performance of the battery-less PRRC is evaluated over the 10 cloudy days.

Figure 13 illustrates the control implementation for a period on 2018 December 24. It can be seen from Figure 13 that with the favor of PV nowcasts, the power curtailment method becomes useful to regulate the ramp-down fluctuations, with the power generation actively curtailed before the actual drops occur. During the specific period, all the 96 ramp-up fluctuations and 49 of 50 ramp-down fluctuations are effectively regulated. The control effectiveness reaches 99.3%, and the energy being curtailed accounts for 4.94% of the total generation. The only ramp violation occurs at 14:07. At this point, a ramp-rate of -105 kW/s is observed, which is very close to the ramp-rate limit. In this case, due to the unavoidable prediction error, the ramp may not be truly recognized. Thus the control is not effectively triggered.

Table 7: Battery-less PRRC performance on the 10 cloudy days.

	Moderate		Highly variable	
	DSTR	SRP-Enet	DSTR	SRP-Enet
nPMAE (%)	8.09	**7.25**	10.08	**9.96**
Control failure (%)	4.01	**3.95**	4.53	**3.58**
Energy curtailment (%)	2.23	**1.66**	**2.89**	3.05

Table 7 shows the control performance over the 10 cloudy days. To validate the effectiveness of the proposed SRP-Enet method on battery-less PRRC application, the state-of-art algorithm developed in [42], namely, dynamic spatio-temporal ramp forecasting (DSTR) is used for benchmarking. Since the DSTR method works only when ramp violations are observed, the metrics except for nPMAE are discarded. It can be concluded that the proposed SRP-Enet method generally outperforms the DSTR algorithm. In both moderate and highly variable days, the SRP-Enet method achieves lower nPMAE and control failure. It is also observed that in the highly variable days, the DSTR method seems to sacrifice less energy. However, this is mainly due to its more control failure. In another word, the energy has not been not fully curtailed to smooth out the ramp-down fluctuations due to the nowcasting inaccuracies. We note that the effective use of DSTR algorithm should require a larger and denser sensor network. However, the feasibility and simplicity are also important considerations for practical application. According to the results presented above, the proposed SRP-Enet method is proved to be more reliable than DSTR when fewer sensors are considered.

6. Conclusion

This paper presents a novel sensor network based PV nowcasting method with the newly developed ST predictor preselection, which can be used for real-time GFC. Compared to the conventional PV nowcasting methods, the main improvements of the proposed method can be summarized as:

1. The proposed SRP preselection establishes a comprehensive predictor preselection mechanism for both spatial and temporal predictors in absence or presence of CSVs.

2. The proposed SRP preselection decomposes the PV dynamics into two scenarios, and the results in two scenarios can be coordinated to provide consistent PV nowcasts at a fixed prediction horizon, with CSV information well contained. Specifically, the use of the developed SRP preselection on different models shows an average nRMSE and nPMAE improvements over 11% and 25% respectively.

3. The proposed SRP-Enet nowcasting reveals strong adaptability under various weather conditions, especially in the highly cloudy days, with an average nRMSE and nPMAE improvements over 13.5% and 41.3% respectively. In addition, it is able to use fewer training data while achieving similar or better results than the benchmarking models which use a larger training set.

The feasibility of integrating SRP-Enet nowcasts to GFC operation is also evaluated through practical experiments. The results show that the use of SRP-Enet nowcasts on battery-less PRRC outperforms the state-of-art algorithm, with less control failures and energy curtailment.

Acknowledgements

This work was supported by the National Natural Science Foundation of China (No. 61803315), Jiangsu Science and Technology Program (BK20180243), AI University Research Centre (AI-URC) through XJTLU Key Programme Special Fund (KSF-P-02 and KSF-A-11), and research development fund of XJTLU (RDF-17-01-28).

Appendix A. Sensor development

The sensor developed herein is based on a 5 cm × 5 cm mini solar cell. Sensing directly using a solar cell shows advantages of presenting more similar characteristics to the target PV systems, e.g. the sensitivities to ambient temperature, humidity, etc. Therefore, the sensor becomes more reliable on detecting CSV impacts with less measurement variances caused by those "non-cloud" factors.

The basic theory behind is that the short-circuit current of a solar cell can present to be quasi-linear to the irradiance it receives [44]. In this sense, once we can measure the instantaneous short-circuit current of the solar cell, and establish an appropriate conversion model, the corresponding GHI can be derived. Given a tuning parameter β and intercept σ, the linearized conversion model can be defined as

$$G = \beta \cdot \frac{G_{STC}}{I_{SCS}} \cdot I_{SC} + \sigma \tag{A.1}$$

where G and I_{SC} are the measured global horizontal irradiance (GHI) and short-circuit current, G_{STC} and I_{SCS} correspond to the solar irradiance and short-circuit current

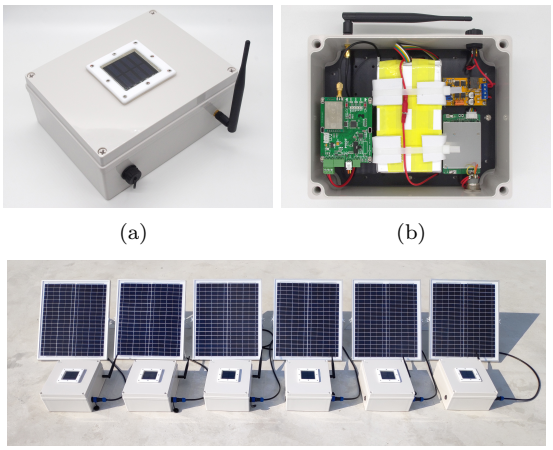

(a) (b)

(c)

Figure A.14: Solar sensor prototype, (a) water-proof shell, (b) inside configuration, (c) PV panel for self-charging.

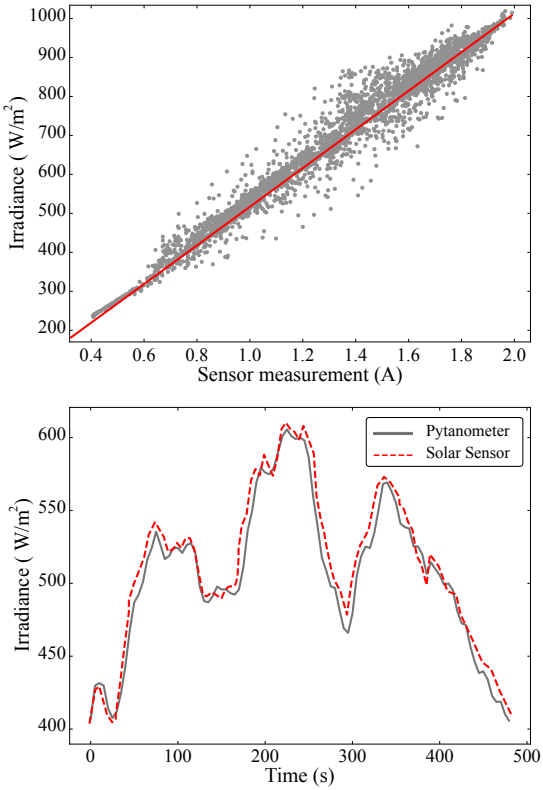

Figure A.15: **Top**. Example of solar sensor calibration with a pyranometer ($\beta = 1.31$, $\sigma = 78.26$). **Bottom.** Comparison of calibrated sensor measurements and pyranometer readings during cloud transitions (temporal resolution of 1 s).

at standard test conditions ($G_{STC} = 1000$ W/m^2 with cell temperature of 25°C or 298 K).

In order to obtain the short-circuit current of the solar cell, a small precise resistor (0.1 Ω) is connected in shunt. In this way, the current through the resistor can approximate to the short-circuit current. For each sensor, the short-circuit current is recorded at 1-s resolution using a STM32 micro-controller, powered by a Li-Po battery. Af-

ter converting the short-circuit current data to GHI using equation (A.1), the data is packed and transmitted to the local server via a LoRa wireless communication module. To assure a consistent and autonomous outdoor operation, the sensor is equipped with a water-proof shell and a PV panel for self-charging, see Figure A.14. The cable-less configuration also provides more flexibilities to the network design.

Regarding the calibration, a commercial pyranometer is placed closely to each sensor, and data from a total of 12 h are used. Figure A.15 shows an example of a single sensor calibration. In this case, the regression parameters β and σ are found as 1.31 and 78.26 respectively. The calibrated sensor measurements are compared with the pyranometer readings over several cloud transition periods, and the mean absolute error is found to be 1.25%. It should be noticed that for a more accurate measurement, the individual cell temperature information is demanded. However, the additional temperature data would occupy more communication channels, and halve the amount of sensors in the network.

References

[1] M. Woodhouse, R. Jones-Albertus, D. Feldman, R. Fu, K. Horowitz, D. Chung, D. Jordan, S. Kurtz, On the path to sunshot: The role of advancements in solar photovoltaic efficiency, reliability, and costs, Tech. rep., National Renewable Energy Laboratory (NREL) (2016).

[2] R. Fu, D. Chung, T. Lowder, D. Feldman, K. Ardani, R. Margolis, U.S. solar photovoltaic system cost benchmark: Q1 2016, Tech. rep., National Renewable Energy Laboratory (NREL) (2016).

[3] M. Karimi, H. Mokhlis, K. Naidu, S.Uddin, A.Bakar, Photovoltaic penetration issues and impacts in distribution network-a review, Sustain. Energy Rev. 53 (2016) 594–605.

[4] M. Diagne, M. David, P. Lauret, J. Boland, N. Schmutz, Review of solar irradiance forecasting methods and a proposition for small-scale insular grids, Renew and Sustan Energy Rev 27 (2013) 65–76.

[5] Energinet.dk, Technical regulation 3.2.2 for pv power plants with a power output above 11 kw, Tech. rep. doc. 14/17997-39 (2016).

[6] Review of prepa technical requirements for interconnecting wind and solar generation, Tech. rep., National Renewable Energy Laboratory (NREL) (2013).

[7] E. Troester, New german grid codes for connecting pv systems to the medium voltage power grid, in: Proc. of 2nd Int. Workshop Concentrating Photovoltaic Power plants: Opt. Design, Prod., Grid Connection, 2009.

[8] H. D. Tafti, A. I. Maswood, G. Konstantinou, J. Pou, F. Blaabjerg, A general constant power generation algorithm for photovoltaic systems, IEEE Trans. Power Electron. 33 (5) (2018) 4088–4101.

[9] A. Sangwongwanich, Y. Yang, F. Blaabjerg, A sensorless power reserve control strategy for two-stage grid-connected pv systems, IEEE Trans. Power Electron. 32 (11) (2017) 8559–8569.

[10] A. Kaur, L. Nonnenmacher, H. Pedro, C. Coimbra, Benefits of solar forecasting for energy imbalance markets, Renew Energy 86 (2016) 819–830.

[11] E. Matallanas, M. Castillo-Cagigal, A. Gutiérrez, F. Monasterio-Huelin, E. Caamaño-Martín, D. Masa, Neural network controller for active demand-side management with pv energy in the residential sector, Applied Energy 91 (2012) 90–97.

[12] X. Yang, M. Xu, S. Xu, X. Han, Day-ahead forecasting of photovoltaic output power with similar cloud space fusion based on incomplete historical data mining, Applied Energy 206 (2017) 683–696.

[13] S. Bacha, D. Picault, B. Burger, I. Etxeberria-Otadui, J. Martins, Photovoltaics in microgrids: An overview of grid integration and energy management aspects, IEEE Trans. Ind. Electron. 20 (1) (2015) 33–46.

[14] L. Liu, Y. Zhao, D. Chang, J. Xie, Z. Ma, Q. Sun, H. Yin, R. Wennersten, Prediction of short-term pv power output and uncertainty analysis, Applied Energy 228 (2018) 700–711.

[15] S. Alessandrini, L. Monache, S. Sperati, G. Cervone, An analog ensemble for short-term probabilistic solar power forecast, Applied Energy 157 (2015) 95–110.

[16] F. Barbieri, S. Rajakaruna, A. Ghosh, Very short-term photovoltaic power forecasting with cloud modeling: A review, Renew Sustan Energy Rev 75 (2017) 242–263.

[17] H. Yang, B. Kurtz, D. Nguyen, B. Urquhart, C. W. Chow, M. Ghonima, J. Kleissl, Solar irradiance forecasting using a ground-based sky imager developed at uc san diego, Solar Energy 103 (2014) 502–504.

[18] C. Zhang, Y. Du, X. Chen, D. Lu, Cloud motion tracking system using low-cost sky imager for pv power ramp-rate control, in: IEEE international Conference on Industrial Electronics for Sustainable Energy Systems (IESES), New Zealand, 2018, pp. 493–498.

[19] C. Zhang, Y. Du, X. Chen, E. Lim, Cloud motion forecasting and cloud base height estimation using two low-cost sky cameras, in: Energy Internet and Energy System Integration (EI2) 2018 2nd IEEE Conference, 2018, pp. 1–6.

[20] E. Scolari, F. Sossan, M. Haure-Touzé, M. Paolone, Local estimation of the global horizontal irradiance using an all-sky camera, Solar Energy 173 (2018) 1225–1235.

[21] J. Zhang, R. Verschae, S. Nobuhara, F. Lalonde, Deep photovoltaic nowcasting, Solar Energy 176 (2018) 267–276.

[22] D. Yang, J. Kleissl, C. Gueymard, H. Pedro, C. Coimbra, History and trends in solar irradiance and pv power forecasting: A preliminary assessment and review using text mining, Solar Energy 168 (2017) 60–101.

[23] M. Lipperheide, J. Bosch, J. Kleissl, Embedded nowcasting method using cloud speed persistence for a photovoltaic power plant, Solar Energy 112 (2015) 232–238.

[24] X. Chen, Y. Du, H. Wen, Forecasting based power ramp-rate control for pv systems without energy storage, in: International Future Energy Electronics Conference (ECCE-Asia), Kaohsiung, 2017, pp. 733–738.

[25] X. Chen, Y. Du, W. Xiao, S. Lu, Power ramp-rate control based on power Forecasting For PV Grid-tied Systems with Minimum Energy Storage, in: The 43rd Annual Conference of the IEEE Industrial Electronics Society (IECON), Beijing, 2017.

[26] S. Achleitner, A. Kamthe, A. E. Cerpa, Sips: Solar irradiance prediction system, ACM/IEEE IPSN.

[27] M. André, S. Dabo-Niang, T. Soubdhan, H. Ould-Baba, Predictive spatio-temporal model for spatially sparse global solar radiation data, Energy 111 (2016) 599–608.

[28] B. Elsinga, W. Sark, Short-term peer-to-peer solar forecasting in a network of photovoltaic systems, Applied Energy 206 (2017) 1464–1483.

[29] D. Yang, Z. Ye, L. Lim, Z. Dong, Very short term irradiance forecasting using the lasso, Solar Energy 114 (2015) 314–326.

[30] A. W. Aryaputera, D. Yang, L. Zhao, W. M. Walsh, Very short-term irradiance forecasting at unobserved locations using spatio-temporal kriging, Solar Energy 122 (2015) 1266–1278.

[31] X. G. Agoua, R. Girard, G. Kariniotakis, Short-term spatio-temporal forecasting of photovoltaic power production, IEEE Trans. Sustain. Energy 9 (2) (2018) 538–546.

[32] D. Yang, On adding and removing sensors in a solar irradiance monitoring network for areal forecasting and pv performance evaluation, Solar Energy 155 (2017) 1417–1430.

[33] V. Fung, J. Bosch, S. Roberts, J. Kleissl, Cloud speed sensor, Atmos. Meas. Techn 7 (1) (2014) 1693–1700.

[34] A. Lorenzo, W. Holmgren, A. Cronin, Irradiance forecasts based on an irradiance monitoring network, cloud motion, and spatial averaging, Solar Energy 122 (2015) 1158–1169.
[35] Y. Chu, B. Urquhart, S. Gohari, H.T J. Kleissl, C. Coimbra, Short-term reforecasting of power output from a 48 mw solar pv plant, Solar Energy 112 (2015) 68–77.
[36] M. Cui, J. Zhang, Estimating ramping requirements with solar-friendly flexible ramping product in multi-timescale power system operations, Applied Energy 225 (2018) 27–41.
[37] R. Inman, H. Pedro, C. Coimbra, Solar forecasting methods for renewable energy integration, Prog. Energy Combust. Sci. 39 (2013) 535–576.
[38] J. Antonanzas, N. Osorio, R. Escobar, R. Urraca, F. M. de Pison, F. Antonanzas-Torres, J. Antonanzas, Review of photovoltaic power forecasting, Solar Energy 136 (2016) 78–111.
[39] H. Pedro, D. Larson, C. Coimbra, A comprehensive dataset for the accelerated development and benchmarking of solar forecasting methods, J. of Renewable Sustainable Energy 11 (2019) 036102.
[40] H. Zhou, Y. Zhang, L. Yang, Q. Liu, K. Yan, Y. Du, Short-term photovoltaic power forecasting based on long short term memory neural network and attention mechanism, IEEE Acess 7 (2019) 78063–78074.
[41] L. M. Hinkelman, Differences between along-wind and cross-wind solar irradiance variability on small spatial scales, Solar Energy 88 (2013) 192–203.
[42] X. Chen, Y. Du, H. Wen, L. Jiang, W. Xiao, Forecasting-based power ramp-rate control strategies for utility-scale pv systems, IEEE Trans. Ind. Electron. 66 (3) (2018) 1862–1871.
[43] M. Saleh, L. Meek, M. A. S. Masoum, M. Abshar, Batteryless short-term smoothing of photovoltaic generation using sky camera, IEEE Trans. Ind. Informat. 14 (2) (2018) 403–414.
[44] M. Muñoz-García, A. Melado-Herreros, J. Balenzategui, P. Barrerio, Low-cost irradiance sensors for irradiation assessments inside tree canopies, Solar Energy 103 (2014) 143–153.